Title
Three-dimensional measurements of the helicon wavelength

Journal
Plasma Sources Science and Technology, 19(4)

ISSN
0963-0252

Authors
Reilly, MP
Miley, GH

Publication Date
2010-08-01

DOI
10.1088/0963-0252/19/4/045006

Plasma Sources Science and Technology

Three-dimensional measurements of the helicon wavelength

To cite this article: M P Reilly and G H Miley 2010 *Plasma Sources Sci. Technol.* **19** 045006

IOP Publishing — Plasma Sources Science and Technology
Plasma Sources Sci. Technol. **19** (2010) 045006 (8pp) doi:10.1088/0963-0252/19/4/045006

Three-dimensional measurements of the helicon wavelength

M P Reilly and G H Miley

Department of Nuclear, Plasma, and Radiological Engineering, University of Illinois at Urbana-Champaign, 104 S. Wright Street, 216 Talbot Laboratory, MC-234, Urbana, IL 61801, USA

E-mail: mreilly@illinois.edu

Received 8 December 2009, in final form 30 March 2010
Published 11 June 2010
Online at stacks.iop.org/PSST/19/045006

Abstract
Full three-dimensional maps of the helicon wave magnetic field are measured. Agreement between the measured and predicted values for the helicon wavelength is discussed and discrepancies are attributed to interpretation of the three-dimensional wave. Magnetic induction probe measurements in *XYZ* space reveal the helicon wave b_z field has both an axial and azimuthal component. Neglecting the azimuthal component underestimates the three-dimensional wave helix by at least a factor of $\sim 2\pi r$, yielding an oversimplified two-dimensional projection. When the wave's azimuthal component is considered, agreement with numerically predicted wavelength values is shown to be within 35%, whereas greater than 100% differences are found when only the two-dimensional wavelength is measured.

(Some figures in this article are in colour only in the electronic version)

1. Introduction

Helicon waves are a form of whistler waves that propagate in a bounded medium, typically plasma. They are right-handed and/or left-handed waves depending on the antenna structure. Additionally, the frequency that drives the wave, ω_{rf}, must be much less than the electron cyclotron frequency ω_{ce} and greater than the ion cyclotron frequency ω_{ci} ($\omega_{\mathrm{ci}} \ll \omega_{\mathrm{rf}} \ll \omega_{\mathrm{ce}}$) [1–6]. The internal plasma magnetic field components, b_r, b_θ and b_z, are most accurately described when a non-uniform radial density distribution is considered. Extensive numerical solutions for these wave fields have been given by Chen [7] and Kramer [8]. The calculated wave fields provide measurable laboratory quantities for the helicon wavelength λ_z and wavenumber k_z.

Previous measurements of the helicon wavelength have been based off the b_z-field on the z-axis centreline of the helicon discharge [9–11]. Axial measurements are performed along the centreline of the plasma discharge for quantifying the helicon wavelength. This method will be shown to be inaccurate because valuable information regarding the axial wavelength is lost in the azimuthal direction. Inclusion of the helix component which contributes to the helicon wavelength may assist in the explanation of why theoretical predictions overestimate this value. A discussion of this overestimation was provided by Franck in 2005 [11] where helicon wavelengths were identified based on b_z scans for a 10 cm diameter tube. Boswell showed similar measurements in 1984 [9] on a 10 cm diameter tube for b_r and b_z with axial scans taken down the discharge centreline while Chen performed a similar measurement [10, 12] on a 5 cm diameter tube with axial b_z profiles. All axial wavelength results were less than the predicted values as calculated from the radial density profiles, dispersion relation and boundary conditions.

When non-uniform radial densities are considered, the boundary condition applied is for finite fields at the origin and a vanishing radial magnetic field component on the wall $b_r(r = a) = 0$, regardless of an insulating or conducting boundary [3]. Application of this boundary condition derived from non-uniform radial profiles is given as

$$\frac{m}{a}\alpha(r = a)b_z(r = a) + k_z\gamma b_z'(r = a) = 0 \qquad (1)$$

as previously derived in [1, 7, 8]. Here, 'a' is the cylindrical tube radius, 'm' is the mode number, 'α' and 'γ' are given by

$$\alpha(r) = \frac{\omega}{k_z}\frac{\mu_0 e n(r)}{B_0}, \qquad (2)$$

$$\gamma = 1 - \left(\frac{k_0}{k_z}\right)^2. \qquad (3)$$

The boundary condition is non-linear, and for given frequency, density and magnetic field, the wave number k_z will uniquely satisfy the expression and an axial helicon wavelength can then be calculated according to

$$\lambda_z = \frac{2\pi}{k_z}. \tag{4}$$

This paper experimentally verifies the axial helicon wavelength. Single axis z-direction scans match previous work; however, these measurements will be expanded to include b_z measurements of the full three-dimensional plasma discharge to more accurately characterize the helicon wave.

2. Experiment

Testing is conducted for a driving frequency $f = 13.56\,\text{MHz}$ at 500 W total input power (typically $P_{\text{FWD}} \cong 515\,\text{W}$ and $P_{\text{RFL}} \cong 15\,\text{W}$; $<3\%$) and 900 G axially applied magnetic field. The field is generated through four glycol cooled electromagnets run at 30 A and 52 V. The magnets physically measure 5.5 inch inner diameter and 11.25 inch outer diameter spanning 18 inch. The gas used is argon at a flow rate of 47 sccm which corresponds to the argon corrected operating pressure of approximately 10 mTorr (facility base pressure of 2×10^{-6} Torr). These were the conditions where previous measurements for the helicon wave profiles match those predicted analytically [1–3, 9]. Three different configurations are tested for a 6.4 cm OD quartz tube (∼5 cm ID). The $m = +1$ antenna is made from a 3/8 inch wide by 0.052 inch thick copper strap with half turn helical antenna lengths of approximately 20, 10 and 5 cm between the circular end rings. This is typically how the antenna length is defined; however, the length is more appropriately defined when the azimuthal component is also considered, i.e. for a half-turn helical antenna

$$l_{\text{antenna}} \cong \sqrt{l_z^2 + [\pi a]^2}. \tag{5}$$

Here, l_z is the distance between the antenna end rings and a is the tube radius. So for an antenna with 10 cm separation between the end rings wound on a 6.4 cm OD cylindrical tube, the antenna length is more appropriately described as

$$l_{\text{antenna}} \cong \sqrt{10^2 + \left[\pi \times \left(\frac{6.4}{2}\right)\right]^2} = 14.2\,\text{cm}. \tag{6}$$

The three antenna tested in this study will therefore be referenced as 22.6 cm, 14.2 cm and 11.2 cm, corresponding to the 20 cm, 10 cm and 5 cm distances between end rings. The antenna lengths and their location within the static magnetic field are shown in figure 1.

Power to the antenna was fed through an ENI A1000 linear amplifier with a Bird 4421 power sensor and a Manitou Systems auto-match network. Argon gas was flowed in the direction of the magnetic field into a 0.5 m diameter, 1 m long stainless steel diffusion chamber. Diagnostic access for magnetic induction probes and RF compensated Langmuir probe measurements are made through a $2\frac{3}{4}$ inch flange on the diffusion chamber while microwave interferometry measurements are performed with a 90 GHz interferometer which straddles the quartz tube. The entire schematic is shown in figure 2 with the electrical RF grounding diagram shown in figure 3. The b-dot probe measurements are made using a Tektronix differential voltage probe so that any noise effects or ground loops are eliminated.

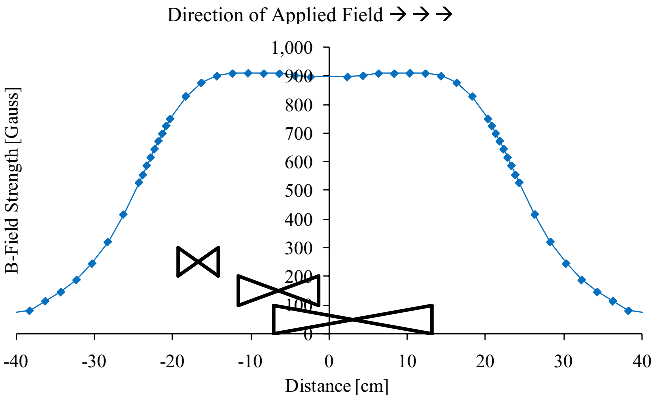

Figure 1. Applied magnetic field with location and lengths of tested antennas.

3. Diagnostics

The diagnostics used to characterize the helicon wave fields (b_r, b_θ, b_z) are magnetic induction probes. These consist of two high frequency surface mount inductors coupled to a centre-tapped transformer so that capacitive plasma pickup is cancelled and that an adequate frequency response is achieved. The complete characterization of the probes with the corresponding impedance frequency analysis can be found in [13].

Often in work with radio frequency plasma discharge, there exists the potential for probes to pick up 'noise' or spurious signal contributions from harmonics of the driving frequency. In the case of plasma driven at 13.56 MHz, harmonics of this fundamental can be found at 27.12, 40.68, 54.24 MHz, etc. These are contributions to the primary signal that are not filtered out by proper probe characterization and not necessarily due to plasma oscillations. To illustrate this point, we consider a raw magnetic probe signal obtained from plasma driven at 500 W with a 900 G applied static magnetic field shown in figure 4. Additionally, we consider the fast-Fourier transform (FFT) of the raw signal in order to view contributions due to harmonics (figure 5).

Immediately obvious from figure 4 is that the signal obtained is not a pure sinusoid. It has slight distortions due to frequency harmonic contributions. Similarly, figure 5 shows clear contributions at the third and fifth harmonics; 40.68 MHz and 67.80 MHz, respectively. In order to accurately report what the fundamental (13.56 MHz) contribution is, a Gaussian fit was applied to the FFT in the vicinity of the fundamental and then the peak value used to calculate the amplitude, taken over the total number of data points, $N = 25\,000$, in these tests. In this case, what appears to be a greater than a 4 V amplitude signal from the raw data is actually a 3.43 V amplitude signal

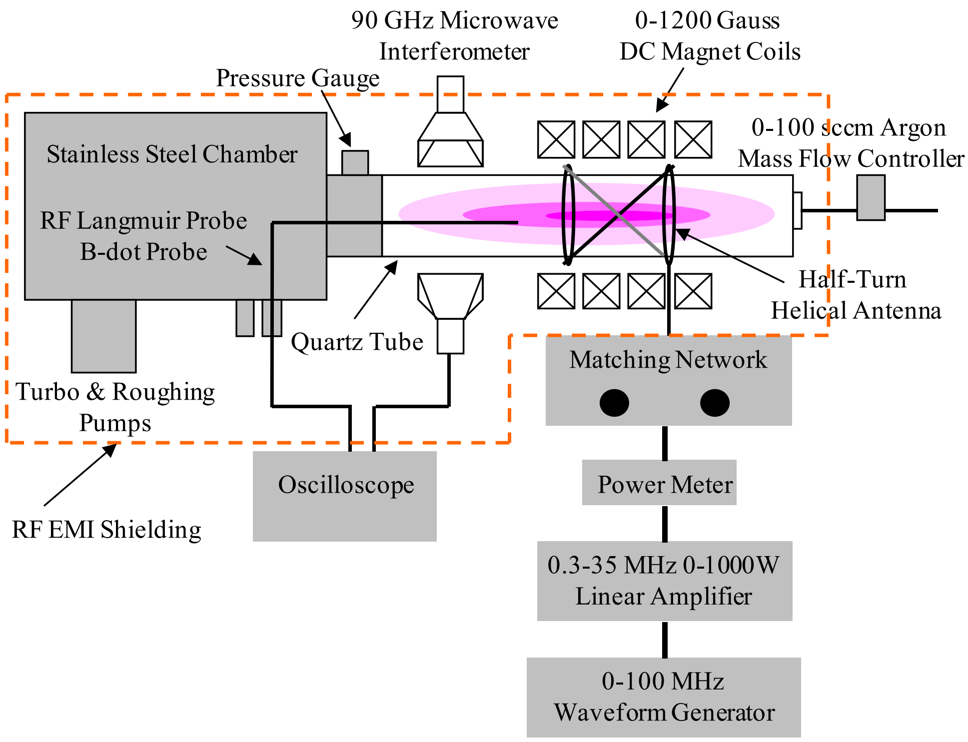

Figure 2. Schematic of AFRL helicon testing facility.

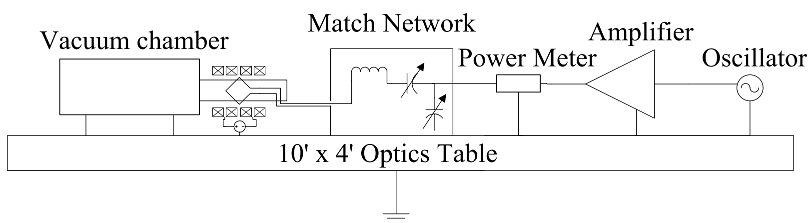

Figure 3. RF grounding and electrical diagram.

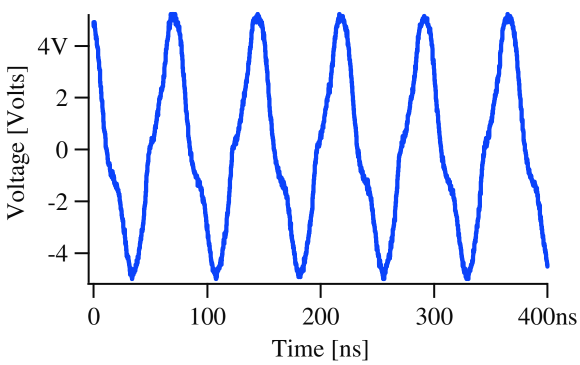

Figure 4. Raw magnetic probe signal for a 500 W, 900 G plasma.

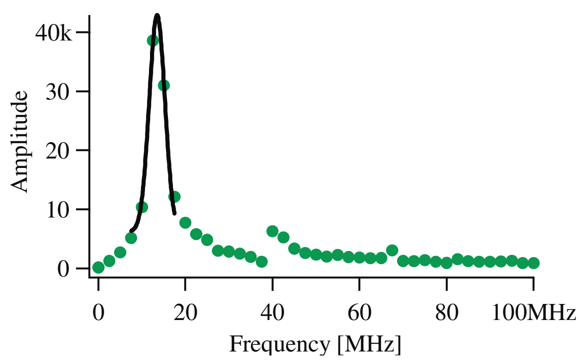

Figure 5. FFT of raw probe signal for a 500 W, 900 G plasma.

when the FFT is analysed; or about a 23% signal measurement error due to frequency harmonics.

As a more demonstrative example of frequency harmonic contribution, we consider a second raw data trace obtained in 100 W 900 G plasma shown in figure 6. The signal appears much more distorted due to harmonic contributions and when we inspect the FFT (figure 7) of the raw data, we find contributions due to the second, third, fourth, fifth, sixth and seventh harmonics. Again, fitting a Gaussian to the fundamental, we can calculate the signal amplitude to be 0.42 V, whereas upon inspection the amplitude may be reported as ∼0.70 V, $(0.90 + 0.50)/2$, or about a 67% signal measurement error.

Obviously, in order to properly interpret results obtained from magnetic probes in plasma, it is necessary to remove any spurious contributions due to frequency harmonics. The most

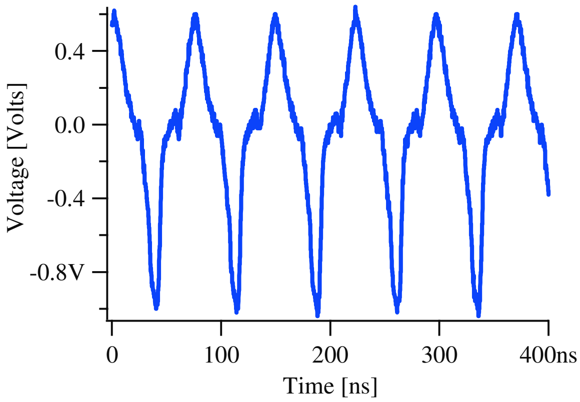

Figure 6. Raw voltage data trace for a 100 W, 900 G plasma.

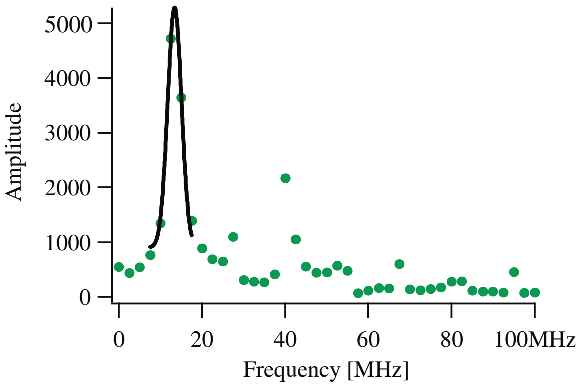

Figure 7. FFT of raw voltage data trace for a 100 W, 900 G plasma.

accurate method to accomplish this is by recording the raw signal, performing a FFT and taking the peak of a Gaussian fit to the area of interest. Although this can often be more time consuming than utilizing an RC integrating circuit before data acquisition in order to directly record the presumed magnetic field amplitude, it is the more accurate approach and allows the user to see harmonic contributions to the signal that will introduce error.

4. Single axis b_z profiles

A routinely used method towards measuring the helicon wavelength has been to take an axial scan and report either the phase difference between the sensing probe and the antenna current or to take the length between successive maxima and minima in the wave amplitude. The successive maxima amplitude method was repeated in this study; however, it is inaccurate in reporting the helicon wavelength even though the results appear correct upon initial inspection. For the 22.6 cm antenna, the results of a single axis scan for the b_z wave field at three different radial 'x' values are shown in figure 8. 'x' here simply refers to a radial location since probes were scanned in an x–y cross section instead of an r–θ direction.

For each scan, a different value for the helicon wavelength is reported, often differing by as much as ~5 cm. The same measurement for the 14.2 and 11.2 cm antenna lengths is shown in figures 9 and 10. In all three cases, the single axis measured

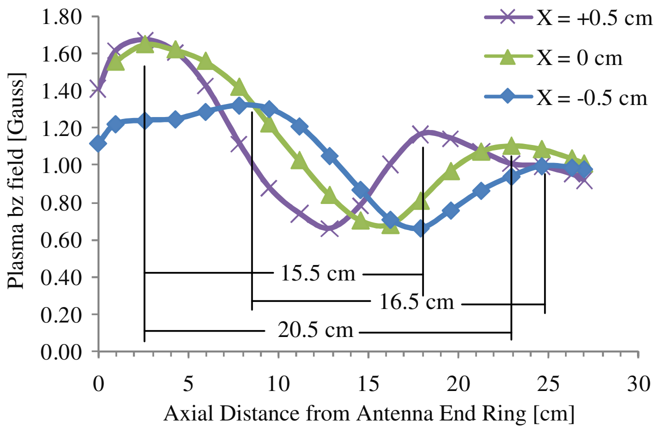

Figure 8. Single axis scan for the b_z wave fields taken at three different radial locations. The antenna length is 27.85 cm.

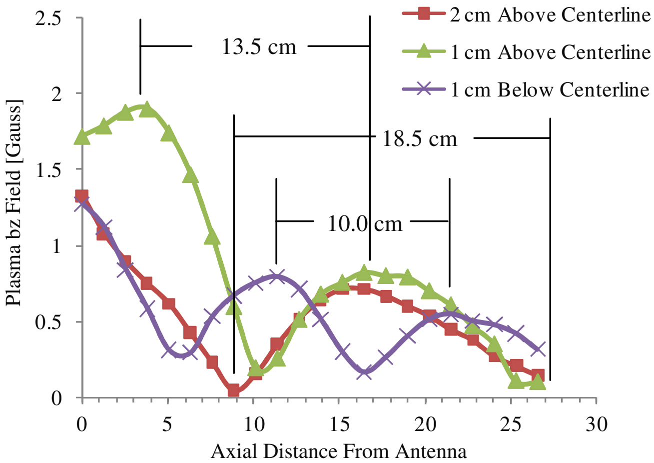

Figure 9. Single axis scan for the b_z wave fields for the 14.2 cm antenna length.

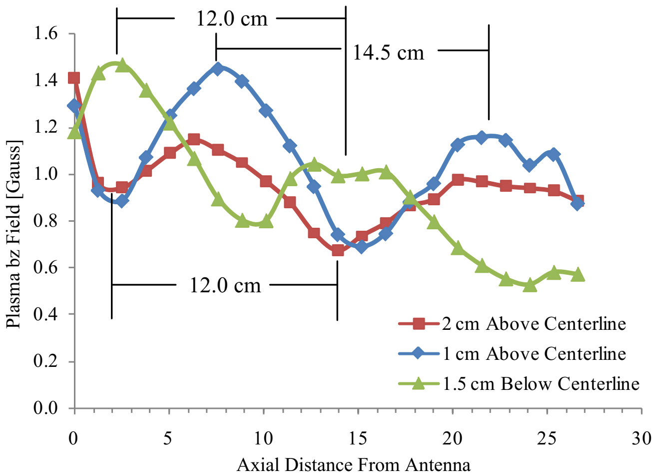

Figure 10. Single axis scan for the b_z wave fields for the 11.2 cm antenna length.

two-dimensional helicon wavelengths are ambiguous. The scans are out of 'phase' depending on where one is performing the measurement and the resulting length is seen to vary by up to 50%.

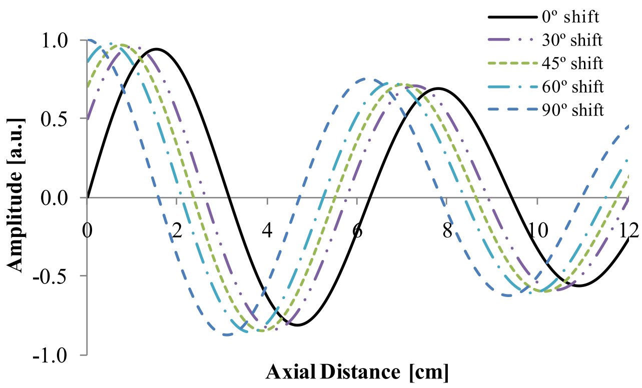

Figure 11. Phase shift for 2D representation of 3D helix.

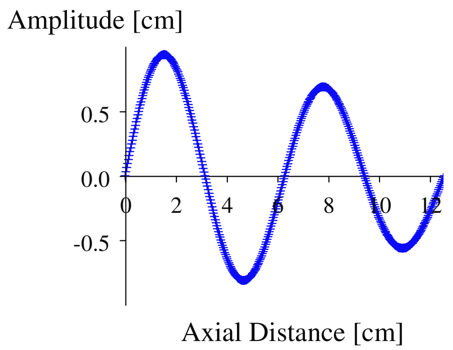

Figure 12. 2D representation of single phase helix.

5. Two- and three-dimensional b_z profiles

The apparent phase differences for the 22.6, 14.2 and 11.2 cm antennas are for the axial z-scans at different radial x,y-locations. Each scan is the consequence of a two-dimensional representation of a helix as demonstrated in figure 11. The result for the helix (which is three-dimensional) is a single wave with a singular associated wavelength. Figure 12 provides an explanation for why previous results of the helicon wave appear to be 'phase' shifted when measured at different radial locations.

When wavelengths have been previously reported based off the two-dimensional single axis scans for the b_z profiles [9, 11, 12, 14–17] they have been reported based off measurements as shown in figures 8–10. However, utilizing the three-dimensional representation of an attenuating wave as modelled in figure 12 (in 2D) and figure 13 (in 3D) as one that linearly decreases in the radial direction from 1 to 0.5 cm over two wavelengths, the actual length of this modelled wave can then be calculated from

$$\lambda_{\rm wave} \cong \sqrt{\lambda_z^2 + \left[2\pi \times \tfrac{1}{2}\,(r_1 + r_2)\right]^2}, \qquad (7)$$

where r_1 is the radius of the wave in the x–y direction at $z = 0$ and r_2 is the radius of the wave at $z = \lambda$, i.e. one axial wavelength downstream. This definition now includes the azimuthal component of the wave. The waves in figures 12 and 13 are exactly the same waves, with figure 12 being the two-dimensional projection. This clearly illustrates how the two-dimensional measurement will underestimate the full wave

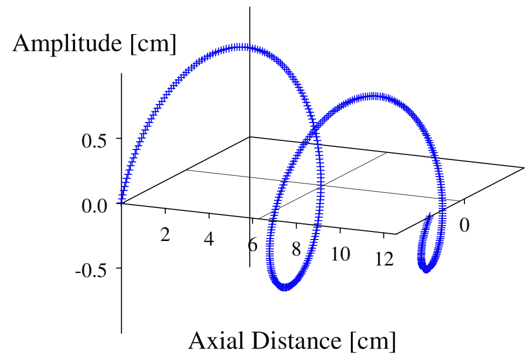

Figure 13. 3D helix represented by the series of 2D phase shifted waves.

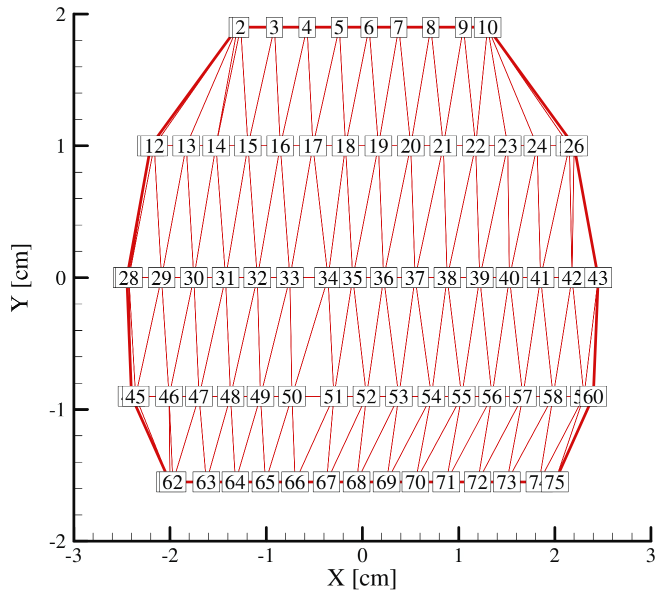

Figure 14. Node-numbering scheme for typical 2D b_z cross-section.

helix. The two-dimensional wavelength is observed to be 6 cm while the three-dimensional wavelength is 6.6 cm; 9% error for this representative case.

Consequently, to image the entire wave, three-dimensional b_z profiles were made at 22 axially separate cross-sections. Each cross section consisted of scans in the XY plane for approximately 75 data points per cross-section or about 1650 data points per three-dimensional contour map. The distance between data points in a cross-section varied between 1.2 and 1.4 mm while each axial cross-section was separated by approximately 1.5 cm. The data point/node-numbering scheme and contour plots were constructed in Tecplot 10. A typical two-dimensional cross-section scheme is shown in figure 14.

The compiled three-dimensional b_z contour plots are shown in figure 15 for the cases of 22.6, 14.2 and 11.2 cm antenna lengths, as previously defined. Red/dark regions correspond to the normalized high b_z field while blue/light regions correspond to normalized low b_z fields. Additionally, two-dimensional (x,z) contour plots in the $y = 0$ plane are shown in figure 16 for b_z. In the case of all three antenna lengths, the edge of the antenna is set at $z = 0$. This is to

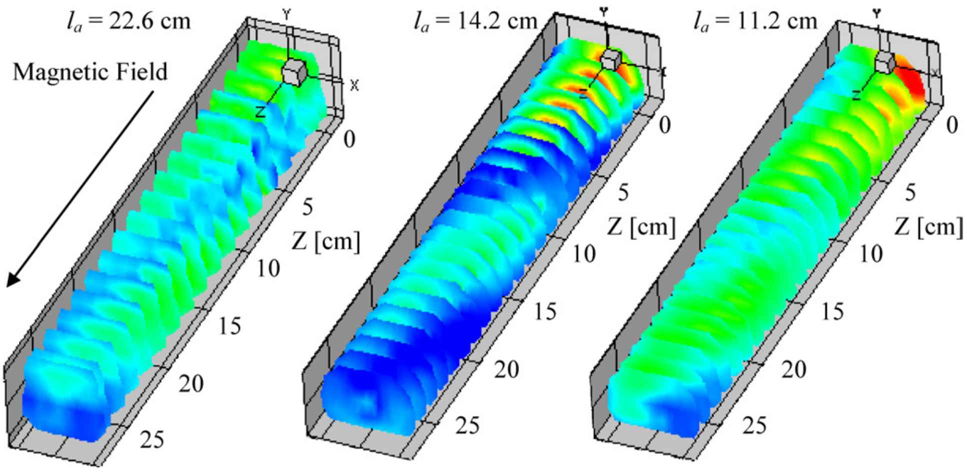

Figure 15. Three-dimensional helicon b_z fields. Antenna lengths: 22.6, 14.24 and 11.19 cm. Antenna edge located at $z = 0$ cm. Wave propagation and static magnetic field in the +z direction. Red/dark regions correspond to high b_z fields while blue/light regions correspond to low b_z fields.

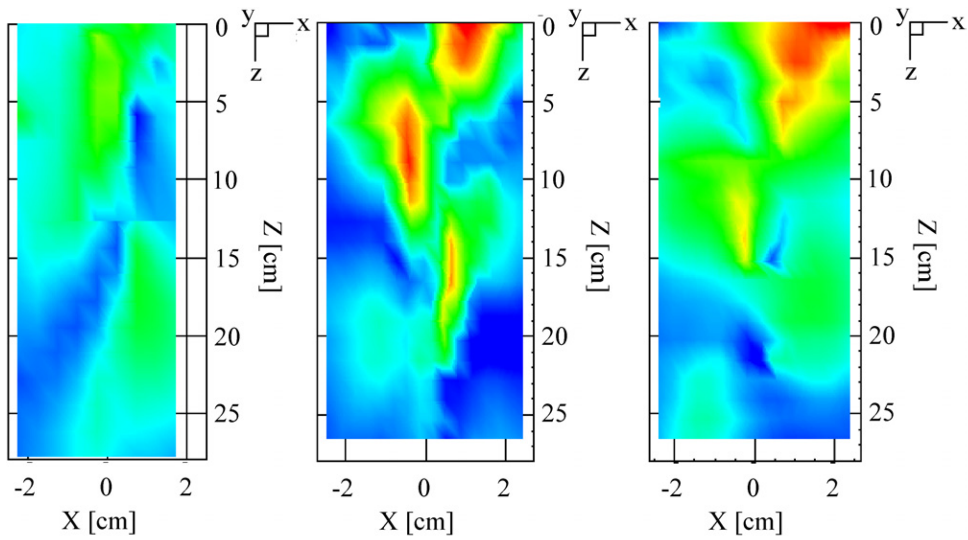

Figure 16. Two-dimensional b_z wave fields taken across centre of tube. Antenna lengths of 22.6, 14.2 and 11.2 cm. Antenna location is at $z = 0$ cm and wave propagation and static magnetic field are in the +z direction. Red/dark regions correspond to high b_z fields while blue/light regions correspond to low b_z fields.

facilitate the determination of the helicon wavelength. The actual location of each antenna edge with respect to the applied magnetic field was given in figure 1. As illustrated in figures 15 and 16, the shortest antenna length does not necessarily correspond to the shortest axial wavelength helicon. This is likely due to the 14.2 cm antenna propagating at a resonance with the cylindrical tubes geometric radial dimensions. The antenna couples energy to the plasma more efficiently and exhibits a more defined wave pattern.

From inspection of figures 15 and 16, the helicon wavelengths can be determined by measuring the length between successive maxima (red/dark regions) or minima (blue/light regions). These values in comparison with the antenna length and expected wavelength are given in table 1. Since each antenna is a half turn helical ($m = +1$) antenna, the expected helicon wavelengths are defined by $\lambda_\parallel = 2l_a$.

The expected values should be more accurately determined from the non-uniform radial density profiles which fix the value of k_z. As an example of this, the radial electron density profiles for the 22.6 cm antennas are measured with an RF compensated Langmuir probe and matched with a theoretical Gaussian profile (figure 17). The wavenumbers and wavelengths for each case are then numerically solved.

Table 1. Summary of expected and measured wavelengths.

3D antenna length l'_a (cm)	Expected wavelength $\lambda_\parallel = 2l'_a$ (cm)	Measured axial wavelength (z-direction only) λ_z(cm)
22.6	45.2	~25
14.2	28.4	~15
11.2	22.4	~19

The resulting wavelengths for each profile are shown in figure 18. As would be expected, lower densities and broader Gaussian profiles yield longer anticipated wavelengths. However, the expected wavelengths are still longer than the measured ones reported above. Recall that the wavelengths

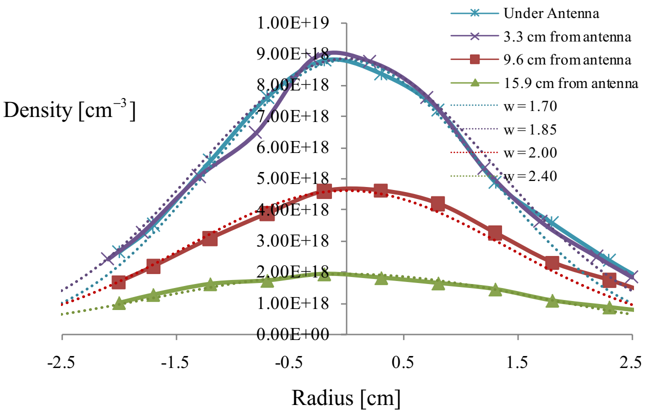

Figure 17. Radial density profiles matched with Gaussian to be numerically solved for the wavelength. The full antenna length is 22.6 cm.

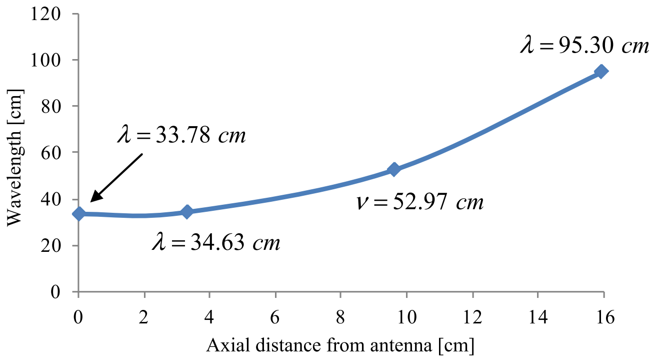

Figure 18. Wavelength solution based on axial varying Gaussian density profiles.

reported in table 1 and, from an inspection of figures 15 and 16, are based solely on the $+z$ directed values and do not yet account for the helical nature (azimuthal component). Additionally, the non-zero values for b_z measured at $r = 0$ are highly repeatable and reproducible. While this differs from the theoretical measurement of a vanishing b_z at $r = 0$, the difference is attributed to numerous simplifications and assumptions in the theoretical derivation, i.e. non-uniform plasma density profiles, diverging axial magnetic field structure, additional wave interactions (TG-waves), plasma drift and diffusion, neutral gas flow, etc.

6. Three-dimensional wavelengths

The 14.2 cm antenna is used as a template for the following analysis. From the contour plots of figure 15, the results indicate the waves have a finite 'thickness' or radius to its structure. This is illustrated more accurately in figure 19 for the 14.2 cm antenna as the wave decreases in radial structure from ∼1 cm at the axial $z = 0$ cm location to ∼0.75 cm one wavelength 'downstream' at $z = 15$ cm. Again, the red/dark regions correspond to the normalized high b_z field regions while the blue/light correspond to the normalized low b_z field regions.

The full wavelength can then be calculated by using a linear decrease in the radial structure (which is valid from the slow damping observed from the 2D profiles of figures 8–10) and taking the average radius over one wavelength to obtain

$$\lambda_{\text{Helicon}} \cong \sqrt{\lambda_z^2 + \left[2\pi \times \tfrac{1}{2}(r_1 + r_2)\right]^2},$$
$$\lambda_{\text{Helicon}} \cong \sqrt{(15)^2 + \left[2\pi \times \tfrac{1}{2}(1 + 0.75)\right]^2}, \qquad (8)$$
$$\lambda_{\text{Helicon}} \cong 16.0\,\text{cm}.$$

This differs from the two-dimensional wavelengths measured in figure 9 (depending on the spatial location of measurement) by anywhere from 16% to 37%. Additionally, it differs from the expected value of 28.4 cm by 78% based off the antenna length expectation. Similar results are obtained for the other two antennas tested where the full three-dimensional wavelengths are ∼25.1 ± 0.5 cm, 16.0 ± 0.5 cm and 19.1 ± 0.5 cm in reference to the 22.6 cm, 14.2 cm and 11.2 cm antennas, respectively.

Although the full measured wavelengths are shorter than those predicted by either the three-dimensional antenna lengths or calculated from radial density profiles, the results demonstrate the helicon wavelength is most accurately represented and measured by three-dimensional imaging. The remaining challenge is to resolve the difference between the theoretically predicted values and those measured in the lab by examining the causes of this discrepancy.

The method of obtaining a k_z based off the non-uniform radial density profiles employs two main assumptions. The first is that the plasma density profile extends all the way to the walls and the second is that the radial profile is constant in the axial direction. We have already shown the radial density profiles in the axial direction are not constant (figure 17), and as a result the axial wavelength will not be either. However, considering the 22.6 cm antenna length where the measured density profile at $z = 0$ predicts a 33.78 cm wavelength (figure 18) and the measured wavelength from three dimensions is 25.1 cm, the difference is 35%. This is in contrast to the two-dimensional measured wavelengths from figure 8 which differ from the predicted result anywhere from 54% to 118%, depending on the chosen two-dimensional scan. Finally, the calculated values for λ_z have a dependence on the magnitude of the measured density profiles. This indicates that error from performing the RF compensated Langmuir probe measurement and analysis could propagate into the calculation of the anticipated helicon wavelengths, i.e. the values may be in better agreement if density measurements were performed with a higher degree of certainty; in this case, the density errors are approximately 40% as a result of standard deviations and probe-sheath impedance ratios.

7. Conclusion

This work provides the first report on three-dimensional imaging of a helicon wave and more generally a plasma wave. Contour plots of the wave's b_z field over a full wavelength for three separate antenna lengths introduced an azimuthal component (axially decaying) which had not been considered before. When the three-dimensional helix is considered,

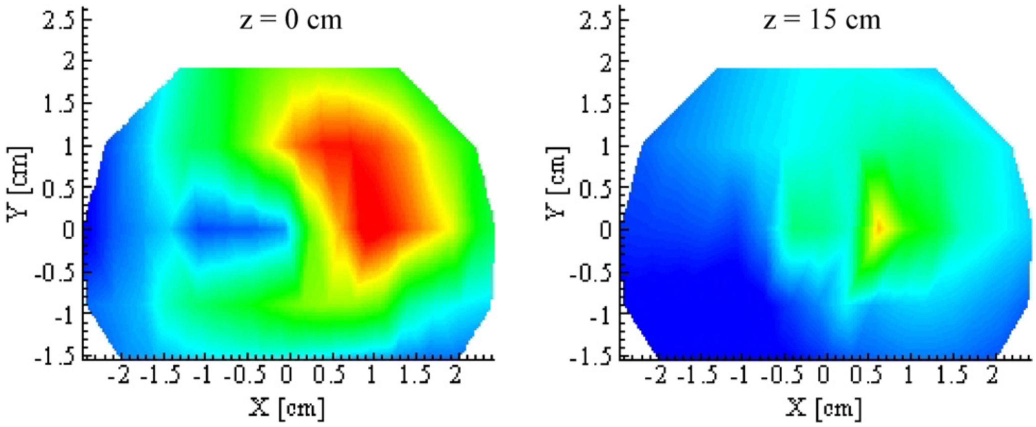

Figure 19. 2D cross sections showing the radial decrease in the wave over an axial length. Radial length decreases from ∼1 cm to ∼0.75 cm over ∼15 cm axially.

agreement with predicted axial wavelength values is achieved to within 35%, contrasted with the >100% differences with two-dimensional measured wavelengths.

The paper also demonstrates the challenges of performing internal plasma measurements. In the case of b-dot probes, the nominal probe size to non-intrusively measure the plasma wave fields had to be balanced against the desire for high probe sensitivity [13]. Post processing of data required performing a Fourier frequency analysis to compensate for spurious signals and remove unwanted harmonics of the driving frequency. If this had not been given thorough attention, large errors in quantifying the wave amplitudes would have been present.

References

[1] Klozenberg J P, McNamara B and Thonemann P C 1965 The dispersion and attenuation of helicon waves in a uniform cylidrical plasma *J. Fluid Mech.* **21** 545–63
[2] Boswell R W 1970 A study of waves in gaseous plasma *PhD Thesis* The Flinders University of South Australia
[3] Chen F F 1991 Plasma ionization by helicon waves *Plasma Phys. Control. Fusion* **33** 339
[4] Chen F F 1992 Experiments on helicon plasma sources *J. Vac. Sci. Technol.* A **10** 13
[5] Sakawa Y *et al* 2003 Plasma production by helicon and slow waves *Phys. Rev. Lett.* **90** 105001
[6] Shoji T, Y S, Nakazawa S, Kadota K and Sato T 1993 Plasma production by helicon waves *Plasma Sources Sci. Technol.* **2** 5
[7] Chen F F, Hsieh M J and Light M 1994 Helicon waves in non-uniform plasma *Plasma Sources Sci. Technol.* **3** 49
[8] Kramer M 1999 Propagation and damping of $m = +1$ and $m = -1$ helicon modes in an inhomogeneous plasma column *Phys. Plasmas* **6** 1052–8
[9] Boswell R W 1984 Very efficient plasma generation by whistler waves near the lower hybrid frequency *Plasma Phys. Control. Fusion* **26** 1147
[10] Chen F F 1996 Physics of helicon discharges *Phys. Plasmas* **3** 11
[11] Franck C M *et al* 2005 Measurements of spatial structures of different discharge modes in a helicon source *Plasma Sources Sci. Technol.* **14** 226
[12] Chen F F, Sudit I D and Light M 1996 Downstream physics of the helicon discharge *Plasma Sources Sci. Technol.* **5** 173
[13] Reilly M P, Lewis W and Miley G H 2009 Magnetic field probes for use in radio frequency plasma *Rev. Sci. Instrum.* **80** 053508
[14] Ellingboe A R and Boswell R W 1996 Capacitive, inductive and helicon-wave modes of operation of a helicon plasma source *Phys. Plasmas* **3** 8
[15] Lehane J A and Thonemann P C 1965 An experimental study of helicon wave propagation in a gaseous plasma *Proc. Phys. Soc.* **85** 301
[16] Light M and Chen F F 1995 Helicon wave excitation with helical antennas *Phys. Plasmas* **2** 10
[17] Tysk S M *et al* 2004 Optical, wave measurements, and modeling of helicon plasmas for a wide range of magnetic fields *PhD Thesis* University of Wisconsin p 40